11(2014) 170 - 184

Latin American Journal of Solids and Structures

www.lajss.org

Finite Element Analysis for Mechanical Characterization of 4D Inplane Carbon/Carbon Composite with Imperfect Microstructure

Abstract

Finite element mesh of multi-directional 4D carbon/carbon (C/C) composite was reconstructed from 2D images obtained by X-ray tomography. Thus, imperfections in the composite such as voids, misalignment and cross-section distortion of the fibre bundles were directly incorporated in the finite element mesh. 2D images of the composite were also used for the characterization of the porosity in the composite. The effect of these micro structural imperfections was studies by assuming perfect bonding at the bundle/matrix interface. The initial mechanical properties of the composite were obtained from unit cell analysis using asymptotic homogenization and moduli in x, y and z directions were 39, 25 and 44 GPa. However, matrix and bundle/matrix interfacial cracks were also clearly visible in the X-ray tomographic images. Later, the effects of debonding was incorporated by using frictional cohesive interaction at bundle/matrix interfaces and matrix cracking was modeled by degrading the elastic properties of matrix. Final, the response of the composite was studied under six individual load cases.

Keywords

Carbon/Carbon composites; Homogenization; X-ray tomography reconstruction; Image based FEM; Cohesive surfaces.

Rajneesh Sharma*
Atul Ramesh Bhagat
Puneet Mahajan

Department of Applied Mechanics,
Indian Institute of Technology Delhi,
New Delhi 110016, India

Received in 06 Oct 2012
In revised form 03 May 2013

*Author email: rajnish0007@gmail.com

1 INTRODUCTION

The multi-directionally reinforced carbon/carbon (C/C) composites are extensively used in aerospace industry due to their high performance mechanical properties. These composites have significant damage induced during the manufacturing process (Jortner (1986), Sharma (2012), Siron (1998)). Damage in the form of matrix cracking, debonding of fiber/matrix and fiber bundle/matrix interfaces occurring during manufacturing, affects the properties adversely (Sharma (2012), Rao $(2008)_{ab}$). These imperfections in the composite were broadly divided into two categories, local and global imperfections. Local imperfections contained defects like voids and cracks, whereas global imperfections were referred to cross-sectional distortions and misalignments. The voids and cracks

are the dominating defects in the composite. Some of these imperfections can be considered directly in the analysis by obtaining the finite element (FE) mesh from X-ray tomographic images. This technique of analysis is called as image-based finite element analysis. Many applications of this approach for reconstruction of FE mesh are found in the area of biomechanics, metal matrix composite, foam, and cement paste (Magne (2006), Wolodko (2000), Youssef (2005), Hain (2008)).

A 3D FE mesh of the composite obtained by using X-ray micro tomography was used by Aubard et al. (2000) and Szeremi et al. (2008) for the analysis of C/C composite. Piat et al. (2006, 2009) obtained 3D structural information of voids for C/C laminates using X-ray computed tomography images and predicted the effective elastic properties of the carbon felts by involving statistical analysis of the microstructure of pores. Vorel et al. (2010) reconstructed the statically equivalent unit cell for plain weave C/C composite from X-ray tomography for homogenization.

Ali et al. (2009) simulated the tension test using ideal and reconstructed FE meshes of the microstructure of plane woven C/C composite. The mechanical properties used for the constituents were determined by nanoindentation test. Sharma et al. (2010) studied the effect of the variation in the microstructure of 3D C/C composite on the mechanical properties by reconstructing FE mesh form X-ray tomographic images. The asymptotic homogenization technique with periodic boundary condition was used for the analysis of the reconstructed unit cells to determine the mechanical properties. The volume average properties of the unit cells were considered as the effective homogenized properties of the composite. The bundles/matrix interfaces were assumed perfectly bonded in the studies discussed above. Sharma et al. (2012) have introduced the cohesive surface interactions at the bundle/matrix interfaces of the reconstructed FE mesh for the simulations of fiber bundle push-out test.

In present study, the inherent micro-structure of the 4D C/C composite was reconstructed by using X-ray tomography. The 2D images obtained from X-ray tomography were used to reconstruct 3D FE mesh having some of the imperfections such as distortion of the fiber bundles and voids. Asymptotic homogenization with periodic boundary conditions was used for unit cell analysis of the composite for perfectly bonded interfaces. Next, matrix cracking was modeled by degrading the elastic properties and interfacial damage was modeled using frictional cohesive surfaces. The response of the unit cells under six individual load cases was studied. The results were compared to the experimental data available in literature.

2 COMPOSITE MATERIAL

C/C composite consists of circular bundles in four directions with nearly 80% volume fraction of fibers. The architecture contains 0/60/120 inplane bundles in xy plane and z-directional bundles in out of plane. C/C composite under consideration was prepared by pitch based matrix impregnation. The coal-tar pitch was used as precursor and carbonization was carried out under high pressure nearly 100 MPa and at 1000 ^{o}C (Devi and Rao (1993)). The graphitization temperature for the composite was nearly 2200 ^{o}C. Specimens for the X-ray tomographic observations were taken from the random locations in a composite block. The reconstructed 2D images of the composite using X-ray tomography are shown in Fig.1. 2D images had clearly relived the presence of different families of the cracks in the composites. In addition to earlier classification of cracks one new family of

cracks (cracks joining to adjacent voids) was observed in these images (see Fig.1). The intra bundle cracks were also observed at some locations as shown in Fig.1a.

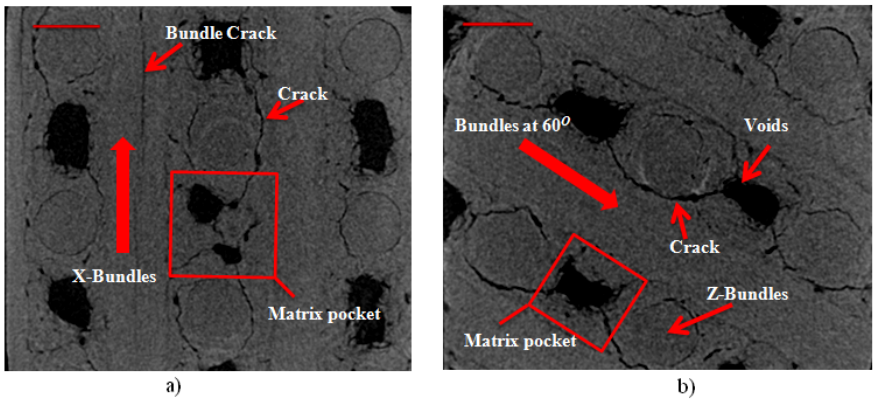

Figure 1 Reconstructed 2D images of the 4D C/C composite a) cross section showing x and z bundles, b) cross section showing bundles at 60^o and z directions.

Interfacial cracks around the z-bundles were observed propagating though matrix and merging with voids at some locations (see Fig.1b).

The voids were observed all most in all the matrix pockets and therefore, can be considered as periodically distributed in the composite. However, the size and shape of the voids differs in each pocket. To have an overall idea of the size and shape of voids in the composite, structural parameters such as thickness distribution and structural model index (SMI) were measured using commercial software "CTvol" (SkyScan 1172). The typical distribution of the structure thickness is given in the Fig.2. The contribution of the thickness less than 100 µm is around 30%. The Structure model index of the voids was nearly 4, which shows that the voids were spheres. The volume fraction of the voids was nearly 2-3% in the composite.

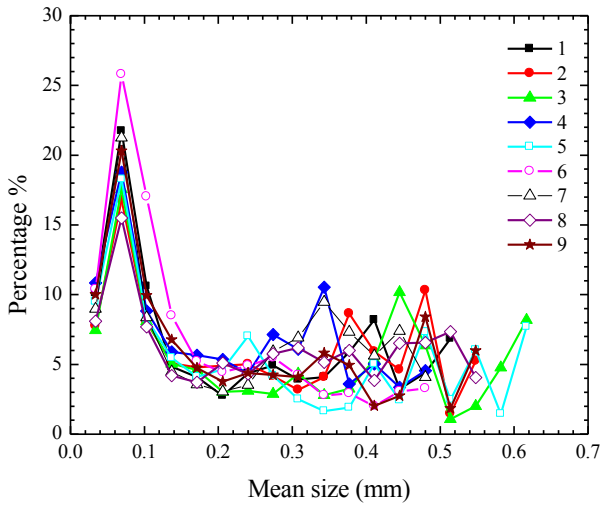

Figure 2 Frequency distribution of the mean structure thickness of the voids.

The 2D images of the composite were also utilized to reconstruct the finite element FE mesh of the unit cells of composites as discussed in next section.

3 RECONSTRUCTED FE MESH

A 3D image of the composite was reconstructed from the 2D images and three randomly chosen unit cells of the composites were cropped. The segmentation process of the constituent was discussed in detail by Sharma at al. (2010). The volume fraction of the constituents in the unit cells is given in Table 2.

Table 1 Volume fraction of the constituents.

Sample	X-fiber	60^0-fiber	120^0-fiber	Z-fiber	Matrix	Voids
A	10	8.5	8.3	12	59.5	1.7
B	8	8.2	7.8	11.8	62.2	2
C	9	9.3	9.5	11.8	58	2.4

Micro cracks present in matrix were ignored during the reconstruction of the 3D image as a fine mesh needed in their vicinity which increases the number of elements drastically and FE mesh obtained was computationally uneconomical. However, the effect of the matrix cracking was considered by degrading the material properties and bundle/matrix interfacial cracks were modeled by frictional cohesive interactions. The reconstructed finite element meshes of three randomly chosen unit cells are shown in Fig.3.

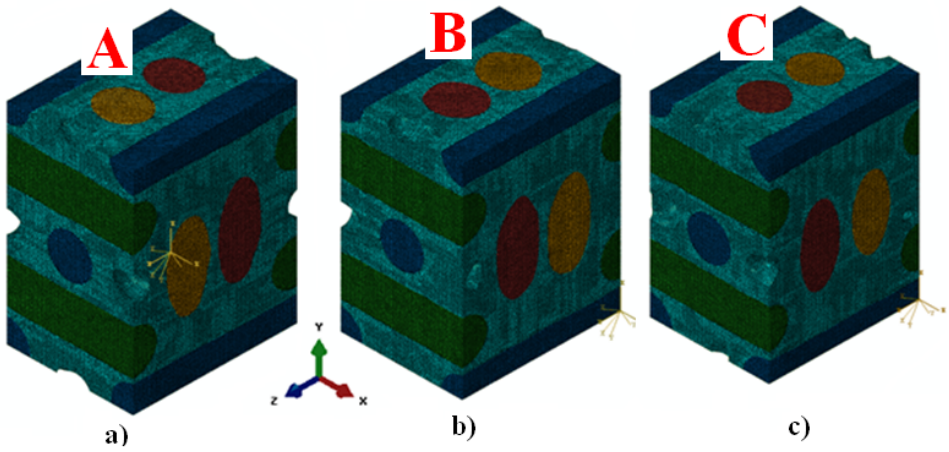

Figure 3 FE meshes for randomly chosen unit cells.

The obtained FE mesh of composite had nearly 10,50,000 first order tetrahedral elements. The bundle/matrix interfaces were considered as perfectly bonded initial to study the effect of the variation in the micro structure in the composite. Next, the bundle/matrix interfaces were assumed connected throughout with frictional cohesive surfaces interaction and the effect of interfacial damage

was studied for six independent load cases. The material properties of the constituent were taken from the work of Rao at el. $(2008)_b$ and are given in Table 2.

Table 2 Effective properties of fibre bundle and matrix GPa

Material	E_{11}	$E_{22}=E_{33}$	$G_{12}=G_{13}$	G_{23}	$\nu_{12}=\nu_{13}$	ν_{23}
	GPa					
Fibre bundle	230	19	23.63	7.6	0.2	0.34
Matrix	19	-	7.92	-	0.2	-

4 HOMOGENIZATION AND PERIODIC BOUNDARY CONDITIONS

Three reconstructed unit cells of the composite were analyzed using asymptotic homogenization and periodic boundary conditions. In this technique, the composite was considered homogeneous at full length scale and inhomogeneous at local scale. The macro scale constitutive relation can be defined by the eqn.1 using asymptotic homogenization (Rao $(2008)_b$, Stefan (1992)).

$$\left\langle \sigma_{ij} \right\rangle = C^H_{ijkl}(e\ )\left\langle e_{kl} \right\rangle \tag{1}$$

Here, C^H_{ijkl} is the homogenized stiffness matrix, which is a function of micro-strain. $\left\langle e_{kl} \right\rangle$ is the volume average strain tensor and $\left\langle \sigma_{ij} \right\rangle$ is the volume average stress tensor.

$$\left\langle \sigma_{ij} \right\rangle = \frac{1}{|v|}\int_v \sigma_{ij}\, dv \tag{2}$$

$$\left\langle e_{ij} \right\rangle = \frac{1}{|v|}\int_v e_{ij}\, dv \tag{3}$$

Here, v is the volume of the RVE. In case of imperfect bonding at the interface the above equation of the average strain can be modified as given below (Rao $(2008)_b$, Stefan (1992)).

$$\left\langle e_{ij} \right\rangle = \frac{1}{|V|}\left[\int_{v_f} e_{ij}\, dv + \int_{V_m} e_{ij}\, dv\ + \frac{1}{2}\int_{s^m/s^f} \left(\left[u_i \right] n_j + \left[u_j \right] n_i \right) ds \right] \tag{4}$$

Here, v_f, v_m and s correspond to fiber, matrix and interface domains in the unit cell. $\left[u_i\right]$ is the jump in the displacement components across the fiber bundle/matrix interface with outward normal n_i. The bundle/matrix interfaces in the composite was modeled by using cohesive surface interactions and node to surface contact algorithm as inbuilt in "Abaqus Standard" (Abaqus 6.10). The unilateral contact and adhesion conditions in the normal directions are given as (Alfano (2006), Sharma (2013)).

$$\tau_1(x)-\left(1-\omega_{\text{int}}(x)\right)K_1\delta_1(x) \;\leq\; 0; \tag{5}$$

or $\delta_1(x) \geq 0;$

$$\text{and}\left\{\tau_1(x)-\left(1-\omega_{\text{int}}(x)\right)K_1\delta_1(x)\right\}\delta_1(x) \;=\; 0; \tag{6}$$

Here ω_{int} is the interfacial damage parameters. K_1 and K_2 are stiffness in the normal and tangential directions, respectively. The tractions law in pure shear is governed by following equations

$$\tau_2(x)=\tau_2^a(x)+\tau_2^f(x), \tag{7}$$

$$\tau_2^a(x)=\left(1-\omega_{\text{int}}(x)\right)K_2\delta_2(x) \tag{8}$$

$$\tau_2^f(x)=\omega_{\text{int}}(\mu\tau_1) \tag{9}$$

ω_{int} is interfacial damage variable and variation of ω_{int} is given as below;

$$\omega_{\text{int}}=\frac{\delta-\delta^0}{\delta^f-\delta^0}\left(\frac{\delta^f}{\delta^0}\right) \tag{10}$$

The six independent load cases of macro strains (e_{kl}) are applied one by one to obtain the coefficients of the stiffness matrix along with periodic boundary conditions. The periodic boundary conditions were derived from the principles of symmetry as given by Li (2008). The boundary conditions under normal loading conditions are given as

$$\left.\begin{aligned} u\big|_{x=0} &= 0 \;\&\; u\big|_{x=l_x} = l_x\varepsilon_{11} \\ v\big|_{y=0} &= 0 \;\&\; v\big|_{y=l_y} = l_y\varepsilon_{22} \\ w\big|_{z=0} &= 0 \;\&\; w\big|_{z=l_z} = l_z\varepsilon_{33} \end{aligned}\right\} \tag{11}$$

here 1, 2, and 3 corresponds to x, y and z direction. u, v and w are the displacements and l_x, l_y and l_z are the lengths of unit cell in x, y and z directions. The boundary conditions under shear loading are given in eqns. (4-6).

$$\left.\begin{aligned} u\big|_{x=0} &= 0 & u\big|_{x=l_x} &= 0 \\ u\big|_{y=0} &= w\big|_{y=0} = 0 & u\big|_{y=l_y} &= w\big|_{y=l_y} = 0 \\ u\big|_{z=0} &= v\big|_{z=0} = 0 & u\big|_{z=l_z} &= 0 \;\&\; v\big|_{z=l_z} = l_z\gamma_{23} \end{aligned}\right\} \tag{12}$$

$$\left.\begin{aligned} v\big|_{x=0} &= w\big|_{x=0} = 0 & v\big|_{x=l_x} &= w\big|_{x=l_x} = 0 \\ v\big|_{y=0} &= 0 & v\big|_{y=l_y} &= 0 \\ u\big|_{z=0} &= v\big|_{z=0} = 0 & u\big|_{z=l_z} &= l_z\gamma_{13} \;\&\; v\big|_{z=l_z} = 0 \end{aligned}\right\} \tag{13}$$

$$\left.\begin{aligned} v\big|_{x=0} &= w\big|_{x=0} = 0 & v\big|_{x=l_x} &= w\big|_{x=l_x} = 0 \\ u\big|_{y=0} &= w\big|_{y=0} = 0 & u\big|_{y=l_y} &= l_y\gamma_{12} \;\&\; w\big|_{y=l_y} = 0 \\ w\big|_{z=0} &= 0 & w\big|_{z=l_z} &= 0 \end{aligned}\right\} \tag{14}$$

The six loading cases in terms of macroscopic strains along with above six boundary conditions were applied to obtained homogeneous stiffness matrix. The results obtained for three unit cells are discussed in next section.

5 RESULTS AND DISCUSSION

5.1 Perfectly bonded interfaces (Case-1)

The effective homogenized stiffness properties of the three randomly chosen unit cells are given in Table 3. The volume average of the properties of unit cells were considered as the effective homogenized properties (EHP) for the composite and are given in Table 3 with associated standard deviation (SD). The obtained stiffness coefficients revealed full anisotropy of the composite. The shear-extension and shear-shear couplings were very small as compare to extension-extension couplings, hence neglected.

Table 3 Mechanical properties of the composite (Here E and G are in GPa).

Sample	E_{11}	E_{22}	E_{33}	ν_{12}	ν_{13}	ν_{23}	G_{12}	G_{13}	G_{23}
	GPa						GPa		
A	38.36	25.11	44.27	0.317	0.083	0.098	7.87	6.64	7.75
B	37.18	25.88	43.77	0.326	0.087	0.097	6.59	7.32	6.36
C	34.32	24.55	43.86	0.311	0.083	0.095	6.86	7.25	6.63
EHP	36.62	25.18	43.97	0.318	0.084	0.097	7.11	7.07	6.91
SD	1.7	0.55	0.22	0.006	0.002	0.001	0.55	0.31	0.6

Effect of the variation in microstructure of the composite on Young's moduli was within 10%. The Poisson's ratio varied in the rage of 5%. The shear moduli were affected more as compare to other properties and the variation was in the range of 18% among all the unit cells.

5.2 Imperfectly bonded interfaces (Case-2)

The fiber bundle/matrix interfaces in the composite had partially damaged during the manufacturing process. The interfacial cracks were partly propagated through matrix, which makes debonded surfaces highly rough. The interfacial cracks were modeled using cohesive surface interaction between the bundle/matrix interfaces. The bundle/matrix interfaces in the composite for unit cells are shown in the Fig.4.

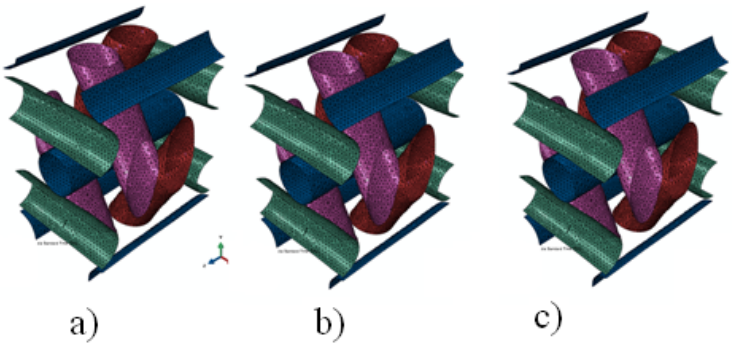

Figure 4 Bundle/matrix interfaces in the unit cells of the composite.

The interfaces of the x and z-bundles are shown in green and blue color respectively. The interfaces of 60 and 120 bundles are in purple and red colors respectively. As shown in Fig.4, the finite

element mesh is smooth at the interfaces and not able to capture roughness amplitudes of the debonded surfaces in the composite. Therefore, a compressive radial stress was applied by expanding the bundle in radial direction to account for the roughness amplitudes of debonded surfaces. The properties for the cohesive surfaces such as coefficient of friction, radial strain, debond strength and fracture energy release rate are given in Table 4. The cracks in matrix were modeled by degrading the properties using linear isotropic damage criterion for damage evolution as inbuilt in "Abaqus Standard" algorithm (Abaqus 6.10). The element stiffness was linearly degraded, once the von-Misses stress reached 20 MPa for the particular element of matrix. The unit cells were analyzed for six independent load cases and are discussed as follows.

Table 5 Interfacial properties for fiber bundle/matrix interface (Sharma (2013)).

Coefficient of friction	Debond strength	Radial strain	Fracture energy
0.75	3	3.87	0.05

5.3 Under e_{11} and e_{33} loading

The stress-strain response of the unit cells is shown in Fig.5 for e_{11} and e_{33} loading conditions. The response of the stresses was nonlinear nearly up to 0.1% strain and followed by an almost linear part up to peek.

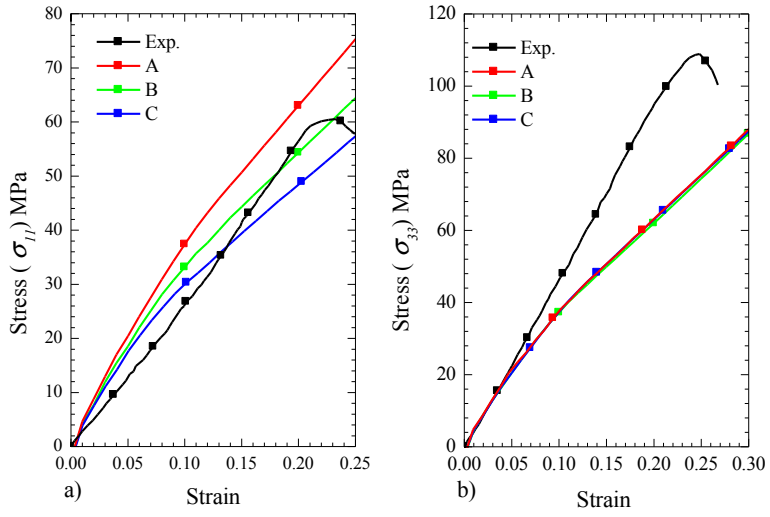

Figure 5 Response under a) e_{11}, and b) e_{33} loading.

The nonlinearity was due to the debonding at the bundle/matrix interfaces and matrix failure. The progressive debonding at the bundle/matrix interfaces was shown in Fig.6 and almost identical for all unit cells. The cohesive surface damage variable (CSDMG) varies from zero for the bonded to one for fully debonded. The red portion of the interfaces as shown in Fig.6 shows the fully debonded elements at the bundle/matrix interfaces. The debonding at the interfaces of the bundles

other than the bundles in x-direction was nearly completed at 0.1% of strain. Also the damage at the interfaces of x-bundles was progressed more than 50% for this strain.

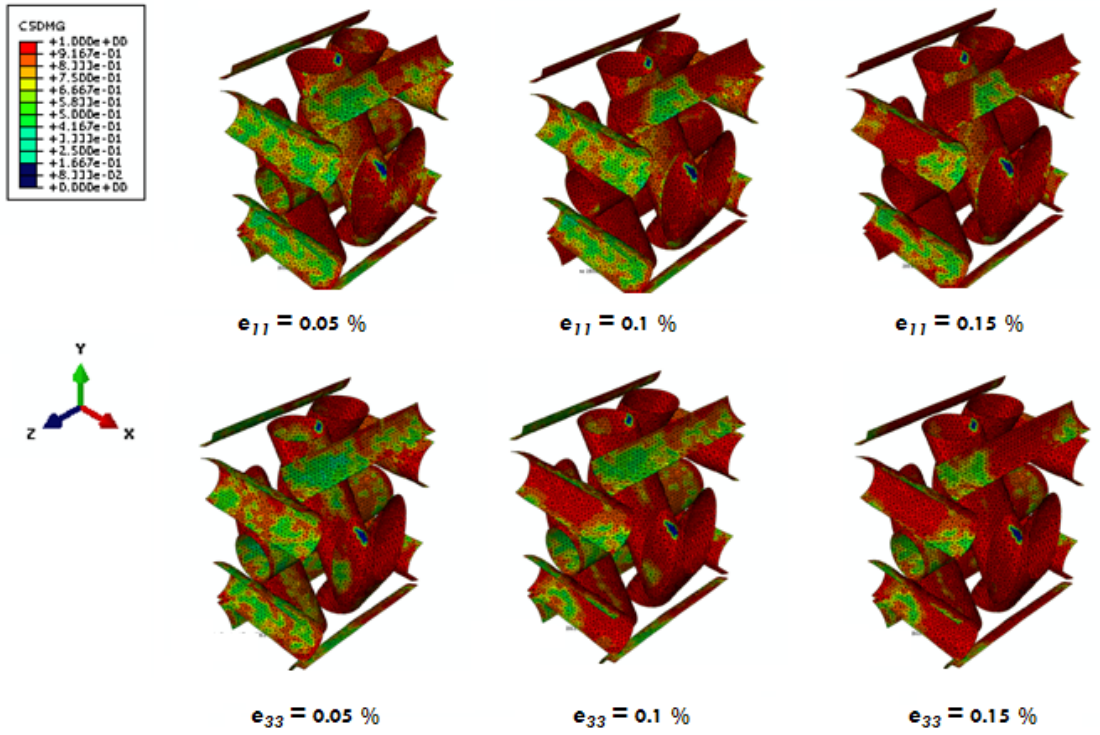

Figure 6 Interfacial damage at the bundle interfaces under e_{11} and e_{33} loading.

The effect of this damage can also be observed from the stress-strain curves shown in Fig.5, because there is a significant degradation in the modulus of the composite up to 0.1%. Further degradation at the x-bundle interfaces was complete up to 0.2% strain and a small effect of this can be observed in the stress-strain curves. The progression of the interfacial damage was observed nearly similar for both cases. The bundles parallel to loading direction had slow progressive damage rather than the bundles in other directions. Hence, the debonding was first completed at the surfaces subjected to mode-I failure and then progressed in mode-II. The stresses in the elements of matrix at some locations were also approached to the failure stress at 0.15 % and the fiber bundle stresses were reached to the failure stress in tension at nearly 0.22%.

5.4 Under e_{22} loading

The response of composite under e_{22} was entirely different as compared to e_{11} and e_{33} load cases. The bundle in 60 and 120 directions had not contributed in the strength because of the week interaction at the bundle/matrix interfaces. The strength of the composite was mostly governed by matrix in this direction. The stress-strain curves of all three unit cells are shown in Fig.7. The response of the curves nonlinear upto the peak followed by a small sudden drop accompanied by an almost decent decreasing slope. Nonlinearity up to the peak was due to progressive debonding of the bun-

dle/matrix interfaces. The interfacial damage at the bundle/matrix interfaces is shown in Fig.8 and almost identical for all unit cells.

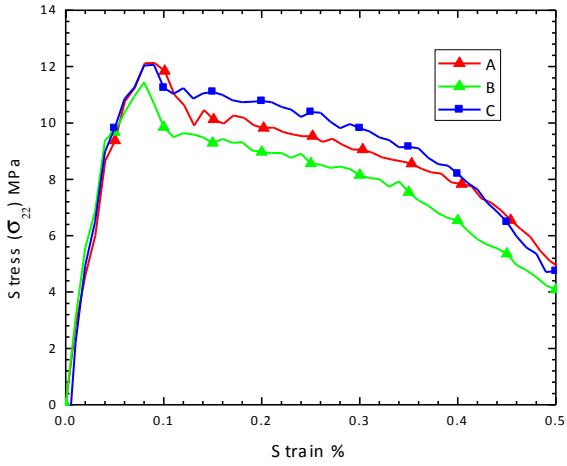

Figure 7 Response of the composite under e_{22} loading case.

As, the surfaces were subjected to mixed mode failure at most of places, the debonding was progressed much faster at the interfaces and nearly completed at 0.1%. The state of damage had not changed in some elements (Ref. green areas of strain increments 0.1 and 0.2 in Fig.8) with further increment of strain. This may be due to the change in the contact at the interfaces.

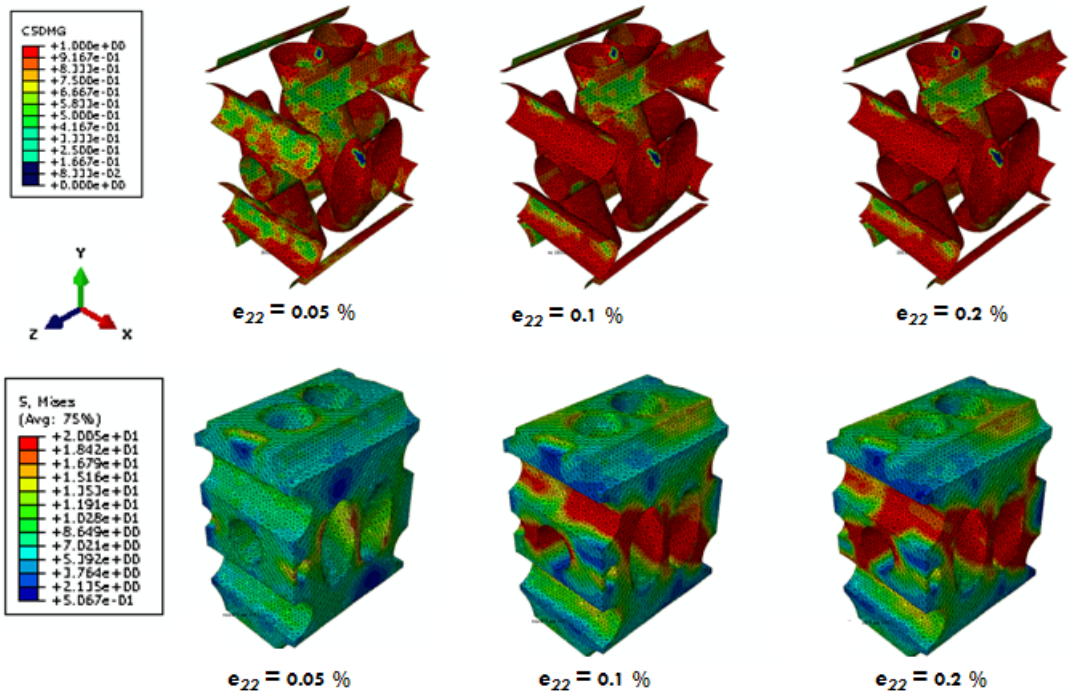

Figure 8 Interfacial damage and matrix stress under e_{22} loading case.

The progression of failure with the stain increments has been shown in Fig.8b. The Misses stress in few elements of matrix was approached to failure strength of matrix at 0.05% strain. Most of elements of matrix along the length of the x-directional bundle have been reached to failure strength at 0.1% strain. The further progression of failure can be observed at 0.2% strain as shown in Fig.8. This means that matrix had started taking loading from 0.5% of strain and at 0.1% of strain sufficient elements of the matrix had reached to the failure stress. This can be confirmed from the strain-strain curves as the peak was falling in between 0.05 and 0.1% strain.

5.5 Under shear loading (e_{12}, e_{13}, e_{23})

Unit cells response under shear loadings was almost identical in all the cases of shear loadings as shown in Fig.9. Figs.9a&c show that shear stress increases nonlinearly up to the peak followed by an almost flat region in case of e_{13} and e_{23}. Whereas in case of e_{12} loading, the post peak curve had an increasing trend in slope (ref. Fig.9b).

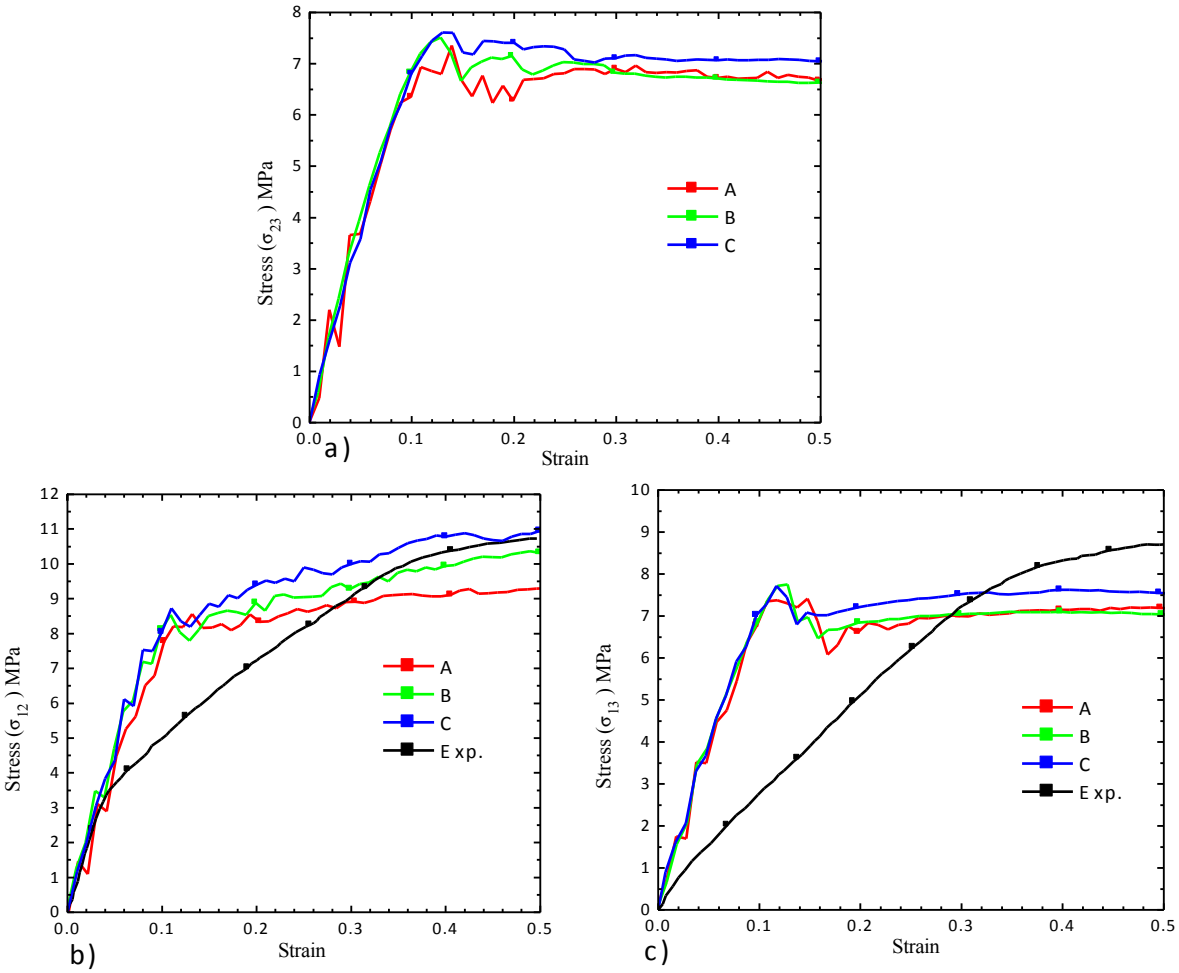

Figure 9 Response of the composite in shear.

The state of damage at the interface and matrix during loading at 0.05 and 0.1 % is shown in Fig10. As one can observe that the interface damage variable (CSDMG) had been reached to maximum value for many nodes present on the bundle/matrix interfaces at 0.05% strain (see the red color on the interfaces in Fig.10a). The further progression of the damage can be observed from Fig.10a As the strain is increased to 0.1%. Most of interfaces had been damaged at 0.1% strain, however at some locations the interfacial surfaces were got locked under compressive contact and therefore no further progression of damage was observed. Mises stress in the elements of matrix at few locations reached to failure strength at 0.05% strain in e_{12} loading case and it had progressed significantly at 0.1% strain (see Fig.10).

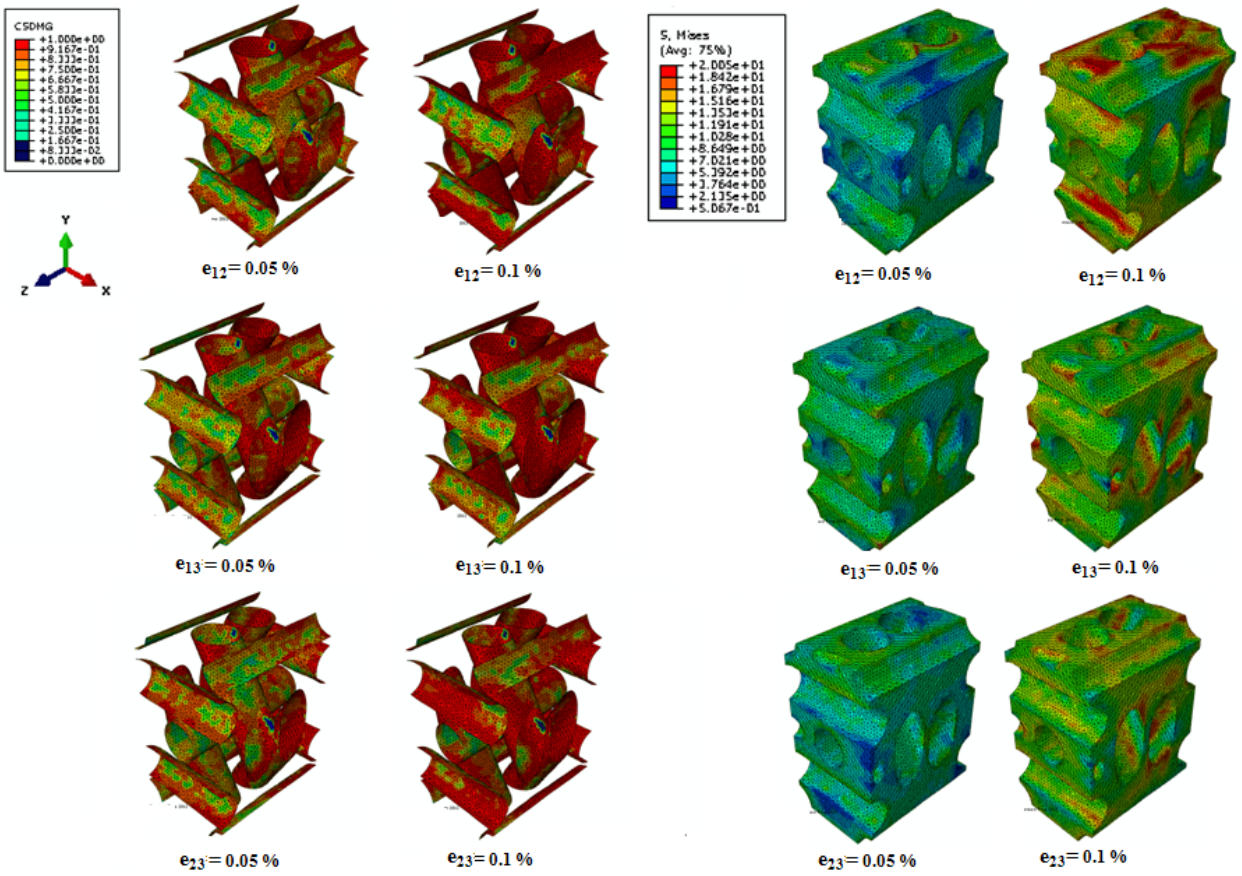

Figure 10 Interfacial damage and Misses stress in matrix under shear loads.

The debonding was nearly completed at 0.1% strain (see in Fig.10) and the peak in the stress-strain curves was also observed near to 0.1%. Therefore initial nonlinearity in the shear stress-strain curves (ref. Fig.9) was mainly due the progression of the damage at the interfaces. In case of e_{12} loading, further increase in the stress from 0.1% strain was due to the contribution of the matrix. The matrix had started taking load due to the contact forces between the 60, 120^o bundles and

matrix. Therefore, stress in the elements of the matrix at some location reached to failure strength (see Fig.10b). In other cases of shear, the contribution of the matrix was less and therefore the stress-strain curves had almost fatter portion in post peak region. The shear behavior of the composite was also compared to the experiment carried out previously by Rao et al. $(2008)_b$. The behavior of the composite was identical to the experiments and shear strength of composite was obtained 7.8 MPa from simulations.

6 CONCLUSION

X-ray tomography was used to reconstruct the microstructure of 4D inplane C/C composite. The finite element meshes were reconstructed for the composite including the defects such as distortion of bundles and voids. Three unit cells were analyzed using asymptotic homogenization technique along with periodic boundary conditions. The effective initial homogenized Young's moduli in x, y, and z directions obtained as 36.93, 25.37, and 44.32 GPa. The variation in the Young's moduli was within 10% whereas shear moduli varied maximum upto 18%. Next, matrix cracking was modeled by degrading the properties of the matrix and interfacial damage was modeled by introducing frictional cohesive surfaces on the bundle/matrix interfaces. The response of the composite was observed under six individual load cases. The strength of the composite observed very low in e_{22} loading and compare to e_{11} and e_{33} in uniaxial tension. This was mainly due to the weak interface between bundle and matrix. The interfaces were observed nearly full debonded at 0.1% strain in almost all load cases. Therefore, the contribution of the fiber reinforcement was very less due to the interfacial damage started from the very early stage of loading.

Acknowledgement Authors are thanks full to snow and avalanche study establishment, Manali for providing the access to the X-ray tomography facility.

References

Abaqus 6.10; http//.www.simulia.com

Alfano G, Sacco E. (2006). Combining interface damage and friction in a cohesive-zone model, International Journal for Numerical Methods in Engineering 68: 542–582.

Ali J, Farooqi JK, Buckthorpe D, Cheyne A, Mummery P. (2009). Comparative study of predictive FE methods for mechanical properties of nuclear composites, Journal of Nuclear Materials 383(3): 247-253.

Aubard X, Cluzel C, Guitard L, Ladevze P. (2000). Damage modeling at two scales for 4D carbon/carbon composites. Computers and Structures 78 (13): 83-91.

Devi GR, Rao KR. (1993). Carbon-Carbon Composites -An Overview. Defence Science Journal 43(4): 369-383.

Hain M, Wriggers P. (2008). Computational homogenization of micro-structural damage due to frost in hardened cement paste, Finite Elements in Analysis and Design 44: 233 - 244.

Jortner J. (1986). Macroporosity and interface cracking in multi-directional carbon-carbons, Carbon 24(5): 603-613.

Magne P. (2006). Efficient 3D finite element analysis of dental restorative procedures using micro-CT data, Dental Material 3(23): 539-548.

Piat R, Tsukrov I, Mladenov N, Guellali M, Ermel R, Beck T, Schnack E, Hoffmann MJ. (2006). Material modeling of the CVI-in¯ltrated carbon felt II. Statistical study of the microstructure, numerical analysis and experimental validation. Composites Science and Technology 66(15): 2769-2775.

Piat R, Bhlke T, Dietrich S, Gebert JM, Wanner A. (2009). Modeling of effective elastic properties of carbon/carbon laminates, Proceedings of Seventeenth International Conference on Composite Materials Edinburgh, UK.

Rao MV, Mahajan P, Mittal RK. $(2008)_a$. Effect of architecture on mechanical properties of carbon/carbon composites, Composite Structure 83:131-142.

Rao MV, $(2008)_b$. Mechanical characterization of multi-directional carbon/carbon composites, Ph.D. Thesis, Indian Institute of Technology Delhi.

S. Li, (2008). Boundary conditions for unit cells from periodic microstructures and their implications, Composites Science and Technology 68: 1962-1974.

Sharma R, Mahajan P, Mittal RK. (2010). Image-based finite element analysis of 3D-orthogonal carbon-carbon composite, Proceedings of the World Congress on Engineering, London, U.K. 2:1597-1601.

Sharma R, Mahajan P, Mittal RK. (2012). Fiber bundle push-out test and image-based finite element simulation for 3D carbon/carbon composites, Carbon 50(8): 2717-2725.

Sharma R, Mahajan P, Mittal RK, (2013). Elastic modulus of 3D carbon/carbon composite using image-based finite element simulations and experiments, Composite Structures, 98: 69-78.

Siron O, Lamon J. (1998). Damage and failure mechanisms of a 3-directional carbon/carbon composite under uniaxial tensile and shear loads, ActaMaterialia 46(18): 6631-6643.

SkyScan 1172, http://www.skyscan.be/home.htm.

Stefan Jansson, (1992). Homogenized nonlinear constitutive properties and local stress concentrations for composites with periodic internal structure, International Journal of Solids and Structures 29(17): 2181-2200.

Szeremi V, Calvo PF, Margetts L, Mummery P. (2008). 3D image-based modeling of a carbon/ carbon composite, 8th World Congress on Computational Mechanics (WCCM8) Venice, Italy: June 30 - July 5.

Vorel J, Zeman J, Sejnoha M, Tomkova B. (2010). Homogenisation of plain weave Carbon/Carbon composite with imperfect microstructure, Submitted to Condensed Matter. http://arxiv.org/abs/1001.4063v3

Wolodko JD, Xia Z, Ellyin F. (2000). Analysis of Al/Al2 O3 metal matrix composites under biaxial cyclic loading using a digital image based finite element method, Material Science and Technology 16: 837-842.

Youssef S, Maire E, Gaertner R. (2005). Finite element modelling of the actual structure of cellular materials determined by X-ray tomography, ActaMaterialia 53: 719-730.